Rare Metals

WILEY | 有科出版 YOUKE PUBLISHING

ORIGINAL ARTICLE OPEN ACCESS

Hollow Porous Nitrogen-Doped Carbon-Confined FeP/Fe_2P Nanoparticle-Armored Catalyst for Efficient Oxygen Reduction Reaction in Aqueous/Flexible Zinc-Air Batteries

Li-Xia Wang[1] | Jia-Sui Huang[1] | Xiao-Yang Cheng[2] | Zhi-Yang Huang[1] | A-Lin Zhou[1] | Shu-Hui Sun[3] | Xiu-Lin Yang[1] | Tian-Xiao Sun[4] | Bin Wu[5]

[1]Guangxi Key Laboratory of Low Carbon Energy Materials, School of Chemistry and Pharmaceutical Sciences, Guangxi Normal University, Guilin, China | [2]State Key Laboratory of Physical Chemistry of Solid Surfaces, Engineering Research Center of Electrochemical Technologies of Ministry of Education, College of Chemistry and Chemical Engineering, Xiamen University, Xiamen, China | [3]Institut National de la Recherche Scientifique (INRS), Center Énergie Matériaux Télécommunications, Varennes, Québec, Canada | [4]Walker Department of Mechanical Engineering, The University of Texas at Austin, Austin, Texas, USA | [5]School of Materials Science and Engineering, Nanyang Technological University, Singapore, Singapore

Correspondence: Xiu-Lin Yang (xlyang@gxnu.edu.cn) | Tian-Xiao Sun (tianxiao.sun@utexas.edu) | Bin Wu (bin.wu@ntu.edu.sg)

Received: 2 July 2025 | **Revised:** 20 September 2025 | **Accepted:** 22 September 2025

Keywords: aqueous/flexible zinc-air batteries | carbon encapsulation | hollow porous structure | oxygen reduction reaction

ABSTRACT

The design of nanoparticles confined in hollow N-doped carbon structures is crucial for improving the oxygen reduction reaction (ORR) kinetics, yet achieving this remains a significant challenge. In this work, hollow porous nitrogen-doped carbon encapsulated FeP/Fe_2P (H-FeP/Fe_2P) were successfully constructed via a templating method combined with dopamine hydrochloride coating, acid etching, and subsequent high-temperature phosphating. In situ spectroelectrochemical investigations and theoretical results demonstrate that the adsorbed hydroxyl species (*OH) can be readily released from the catalyst surface by facilitating the dissociation of oxygen–oxygen bonds at the active sites of Fe, thus accelerating the kinetics of the ORR. The optimized H-FeP/Fe_2P achieves a high limiting current density of 5.5 mA cm^{-2} and a low Tafel slope of 39 mV dec^{-1} in 0.1 M KOH, outperforming corresponding solid samples and most reported transition metal phosphide catalysts. Moreover, the H-FeP/Fe_2P-based aqueous ZAB exhibits remarkable performance, including high peak power density (175 mW cm^{-2}), large specific capacity (813 mAh g^{-1}_{Zn}), and stable charge/discharge stability over 800 h. The corresponding solid-state zinc-air battery also delivers a high peak power density of 101 mW cm^{-2} and excellent flexibility. The carbon confinement strategy proposed in this study opens new avenues for developing high-performance and cost-effective non-precious metal ORR catalysts in zinc-air batteries.

1 | Introduction

In renewable energy conversion systems such as fuel cells and metal-air batteries, the oxygen reduction reaction (ORR) plays a pivotal role [1–4]. However, its inherently sluggish kinetics and high overpotential significantly hinder the energy conversion efficiency and overall performance of these devices [5–7]. Although noble metal Pt-based catalysts exhibit unparalleled ORR activity, their practical implementation is severely hindered by scarcity, prohibitive cost, and stability degradation [8–10]. Consequently, developing non-precious metal alternatives with comparable activity, superior durability, and cost-effectiveness remains a central challenge in contemporary electrocatalysis research [11–15].

Transition metal phosphides (TMPs) have emerged as promising alternatives to Pt-based catalysts, attributed to their tailorable electronic structure, compositional versatility, and

environmental benignity [16, 17]. It was demonstrated that incorporating negatively charged phosphorus with transition metals can localize electronic delocalization and narrow the energy gap of molecular orbitals, thereby enhancing electron transport and accelerating reaction kinetics [18–20]. Among them, iron-based phosphides exhibit unique potential in ORR catalysis by virtue of the high earth abundance and low synthesis cost [21]. However, monophosphate exhibit insufficient intrinsic conductivity. Integrating carbon-based materials significantly enhances electron transfer efficiency, whereas nonmetallic doping can effectively improve conductivity and intrinsic activity [22, 23]. Transition metal-based carbon composites are regarded as ideal alternatives to precious metal ORR catalysts, owing to their high activity, superior durability, and methanol tolerance [24]. Moreover, hollow carbon materials, featuring a distinctive "carbon shell-inner cavity" architecture, exhibit high specific surface area and tunable porosity, attributed to their hierarchical structural design. The inner cavity reduces charge and mass transport distance, whereas the shell mesopores provide diffusion channels for rapid ion transport [25]. In particular, the ultra-thin carbon shell encapsulation strategy is able to form a physical barrier to prevent metal center oxidation and particle aggregation while preserves active site accessibility, thereby significantly improving catalyst stability [24]. However, carbon shell thickness plays a pivotal role in determining the performance of active core-thin shell architecture. Overly thick coatings impede reactant access to active sites, diminishing electrocatalytic performance, whereas insufficiently thin shells fail to offer adequate protection [26]. Therefore, precise tuning of carbon shell-coated transition metal compound catalysts is essential for achieving high activity and durability.

In summary, hollow FeP/Fe_2P nitrogen-doped carbon nanoboxes (H-FeP/Fe_2P) were successfully synthesized via a hard-templating strategy combined with high-temperature phosphorylation. Surface modification of metal oxide templates with dopamine hydrochloride, followed by thermal treatment, incorporated carbon and nitrogen precursors while forming a hollow graphitic carbon shell. This architecture effectively inhibited the migration, aggregation, and dissolution of phosphide, concurrently maintaining high active site accessibility. The uniformly dispersed FeP and Fe_2P nanoparticles provided abundant reaction centers, accelerating electron transfer of transition-state intermediates during the ORR process and significantly enhancing catalytic activity. The H-FeP/Fe_2P demonstrated exceptional ORR performance, achieving a high limiting current density of 5.5 mA cm^{-2}, a kinetic current density of 8.5 mA cm^{-2}, and a low Tafel slope of 39 mV dec^{-1}, surpassing most reported transition metal phosphide catalysts and even commercial Pt/C. Liquid and flexible ZABs assembled with H-FeP/Fe_2P achieved peak power densities of 175 and 101 mW cm^{-2}, respectively, outperforming Pt/C-based counterparts (128 and 57 mW cm^{-2}). The liquid ZAB exhibited negligible performance degradation over 800 h of continuous cycling and retained stable open-circuit voltages under bending angles of 0°, 60°, 90°, and 180°. These results provide a new direction for high-performance low-cost transition metal phosphide-based air cathodes in flexible energy storage devices.

2 | Experimental

2.1 | Materials

Absolute ethanol (C_2H_5OH, 99.7%) was sourced from Sichuan Xilong Science Co. Ltd. Sodium hydroxide (NaOH, 96.0%), ferric chloride hexahydrate ($FeCl_3{\cdot}6H_2O$, ≥ 97.0%), poly(vinylpyrrolidone) ($(C_6H_9NO)_n$, 99.0%, PVP), dopamine hydrochloride ($C_8H_{11}NO_2{\cdot}HCl$, 98.0%), and tris(hydroxymethyl)aminomethane ($C_4H_{11}NO_3$, ≥ 99.8%, tris buffer solution) were purchased from Aladdin Industrial Corporation. Nafion (5.0% solution) was obtained from Shanghai Aladdin Biochemical Technology Co. Ltd. Commercial Pt/C (20.0 wt%) was purchased from Suzhou Sinero Technology Co. Ltd. Potassium hydroxide (KOH, 90.0%) was sourced from Macklin Biochemical Co. Ltd. The RuO_2 powder was synthesized via the calcination of $RuCl_3$ in the air at 400°C. All reagents were employed without further purification.

2.2 | Synthesis of Fe_2O_3 Nanoboxes Precursor

The Fe_2O_3 nanoboxes were synthesized via a facile hydrothermal method. Typically, 50 mL of 5.4 M NaOH solution was added to 50 mL of 2.0 M $FeCl_3{\cdot}6H_2O$ solution at 75°C with stirring, and reacted in a Teflon-lined stainless steel autoclave at 100°C for 4 days. Finally, the resulting product was washed several times with deionized water and ethanol, respectively, and dried in a vacuum at 70°C to afford the reddish-brown Fe_2O_3 nanoboxes.

2.3 | Synthesis of Solid Fe_2O_3@PDA Nanoboxes

Firstly, 500 mg of the synthesized Fe_2O_3 nanoboxes were ultrasonically dispersed in 100 mL of deionized water. Then, 500 mg of dopamine hydrochloride was added under magnetic stirring, followed by the addition of 10 mM Tris buffer solution to adjust the pH to approximately 10. The mixture was stirred at room temperature for 8 h, then centrifuged and dried.

2.4 | Synthesis of Hollow Fe_2O_3@PDA Nanoboxes

Subsequently, the above powder was dispersed in 4 M HCl and allowed to stand at 80°C for 24 h. After centrifugation, it was washed three times with deionized water and then dried in an oven at 80°C.

2.5 | Synthesis of H-FeP/Fe_2P and S-FeP/Fe_2P Nanoboxes

Finally, the solid or hollow Fe_2O_3@PDA samples were mixed and ground with red phosphorus in a mass ratio of 1:2, then subjected to high-temperature phosphating at 900°C for 2 h, with a heating rate of 5°C min^{-1}. The resulting catalysts were designated as S-FeP/Fe_2P and H-FeP/Fe_2P, respectively.

2.6 | Synthesis of Single Fe and Single P Samples

As a comparison, single Fe and P samples were synthesized using similar methods. The synthesis of the single Fe sample was similar to that of H-FeP/Fe_2P, except that red phosphorus was not introduced for direct calcination at 900°C. In contrast, the single P sample was dried by stirring the PDA species at room temperature followed by centrifugation and dried. Subsequently, it was ground together with red phosphorus in a mass ratio of 1:2 and subjected to phosphating at 900°C.

The synthetic samples were modulated by adjusting the etching time, the mass ratio of precursor to red phosphorus, and the phosphating temperature.

3 | Results and Discussion

3.1 | Synthesis and Structural Analysis

As depicted in Figure 1A, Fe_2O_3 nanoboxes fabricated via the template method were polymerized with dopamine hydrochloride under room temperature conditions, yielding Fe_2O_3@PDA with an average size of roughly 500 nm. Subsequently, the Fe_2O_3 cores were etched off in a hot-acidic environment to generate a hollow nanobox structure. Eventually, the hollow FeP/Fe_2P nanoboxes encapsulated with nitrogen and carbon were successfully attained after phosphatization in nitrogen at 900°C for 2 h. The crystal structure of the synthesized catalysts was investigated by XRD. As shown in Supporting Information S1: Figure S2, XRD confirmed the successful synthesis of the Fe_2O_3 nanobox precursor (JCPDS No. 33-0664) [27, 28]. By adjusting the acid etching duration, the ratio of precursor to red phosphorus, and the phosphating temperature, the electrocatalytic performance of the oxygen reduction reaction (ORR) was meticulously optimized. The crystal structure of the synthesized catalysts was investigated by XRD. As shown in Figure 1B, XRD patterns of H-FeP/Fe_2P correspond to the FeP (JCPDS: 39-0809) [29, 30] and Fe_2P phases (JCPDS No. 51-0943) [31, 32]. In addition, a distinct diffraction peak is observed at 21.9°, attributed to the (120) crystal plane of carbon (JCPDS No. 50-0926) [33]. As illustrated in Supporting Information S1: Figure S3, XRD patterns of the catalysts subjected to varying etching durations. Remarkably, the H-FeP/Fe_2P etched for 24 h displayed the utmost crystallinity. Conversely, upon extending the etching time to 48 h, the phosphide peaks nearly vanished, leaving only the carbon peaks. This may be because a short etching duration insufficiently removes Fe_2O_3, whereas excessive etching leads to over-removal and results in poorly crystalline phosphides. Until the etching time was 48 h, Fe_2O_3 was completely removed and failed to form phosphides. The catalysts obtained at different phosphating temperatures were perfectly matched with FeP and Fe_2P (Supporting Information S1: Figure S4). XRD patterns of S-FeP/Fe_2P and H-FeP/Fe_2P are identical, confirming that the two possess the same phase composition (Supporting Information S1: Figure S5a). As shown in Supporting Information S1: Figure S5b,c, XRD pattern of a single Fe sample corresponds to monatomic Fe (JCPDS No. 06-0696) [34], whereas XRD pattern of the single P sample shows only carbon peaks. The Raman spectra of the samples indicated that H-FeP/Fe_2P exhibited higher I_D/I_G values (intensity ratio of D-band and G-band) at 900°C with a mass ratio of 1:2 (Supporting Information S1: Figure S6). Notably, the I_D/I_G ratio for H-FeP/Fe_2P (1.57) is significantly higher than that of S-FeP/Fe_2P (1.17), Fe (1.44) and P (1.43) samples (Figure 1C and Supporting Information S1: Figure S7), indicating a higher defect density in H-FeP/Fe_2P. This increased defect concentration may enhance electron transfer, thereby promoting the electrocatalytic process [35]. In addition, the specific surface area and porosity of the samples were determined using the nitrogen adsorption-

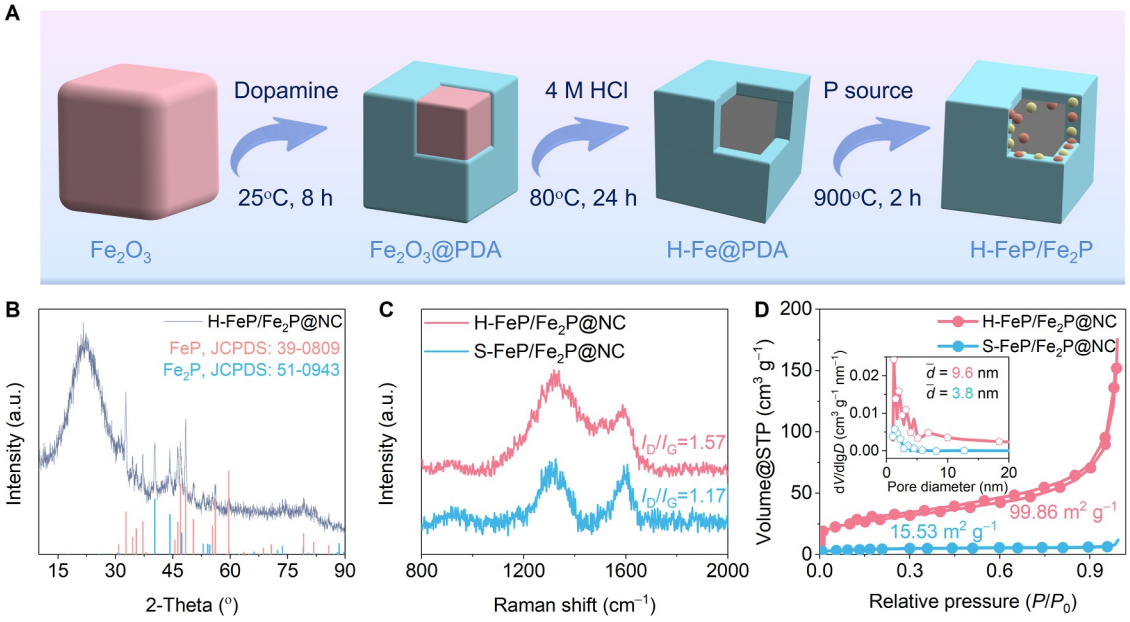

FIGURE 1 | Synthesis and structure characterization of as-prepared catalysts. (A) Schematic illustration of the synthesis of H-FeP/Fe_2P. (B) XRD pattern of H-FeP/Fe_2P. (C) Raman spectra of the as-prepared catalysts, and (D) N_2 adsorption–desorption isotherm of H-FeP/Fe_2P and S-FeP/Fe_2P (inset: corresponding pore size distribution curves).

desorption method. The Brunauer–Emmett–Teller (BET) results (Figure 1D) reveal that H-FeP/Fe_2P has the largest specific surface area (99.86 $m^2\ g^{-1}$), which is 6.4 times higher than that of S-FeP/Fe_2P (15.53 $m^2\ g^{-1}$), indicating more exposed active sites of the hollow structure, conducive to mass and electron transfer in the electrocatalytic process [36]. As shown in the inset of Figure 1D, H-FeP/Fe_2P also exhibited a considerably larger pore size (9.6 nm) than S-FeP/Fe_2P (3.8 nm), indicating enhanced porosity because of acid etching. These results suggest that H-FeP/Fe_2P contribute provide sufficiently abundant reaction centers and mass transfer channels to promote the diffusion and penetration of reaction intermediates in the catalytic process [37].

SEM image in Figure 2A reveals that H-FeP/Fe_2P retains a uniform hollow cubic nanobox morphology. This result is confirmed by transmission electron microscopy (TEM) in Figure 2B, which shows a carbon shell thickness of approximately 51 nm. These results suggest that the hollow structure is well-preserved after carbonization and high-temperature phosphating treatment. High-resolution TEM (HR-TEM) images in Figure 2C–F identify FeP (210) nanoparticles with a lattice spacing of 0.235 nm and Fe_2P (111) nanoparticles with a spacing of 0.224 nm. High-angle annular dark field scanning transmission electron microscopy (HAADF-STEM) in Figure 2G demonstrates that the FeP and Fe_2P nanoparticles are uniformly dispersed with a nitrogen-carbon matrix as the protective shell. The energy dispersive spectroscopy (EDS) results of H-FeP/Fe_2P further confirmed the presence of Fe, P, C, and N in the catalyst (Supporting Information S1: Figure S8). Overall, these results indicate that uniform FeP and Fe_2P nanoparticles are embedded within the carbon nanobox.

X-ray photoelectron spectroscopy (XPS) analysis was performed to elucidate the elemental composition and surface chemical states of the synthesized catalysts. As illustrated in Supporting Information S1: Figure S9, XPS spectrum confirmed the presence of the elements Fe, P, O, C, and N. The high-resolution C 1s XPS spectrum of H-FeP/Fe_2P (Supporting Information S1: Figure S10) clearly resolved distinct peaks of C=C (284.0 eV), C–Ministero dell'Istruzione, dell'Università e della Ricerca C (284.8 eV), C–O (286.1 eV), and C=O (286.2 eV) bonds [38]. Figure 3A shows a weaker Fe 2p XPS signal for H-FeP/Fe_2P, consistent with the lower iron content resulting from HCl etching of internal Fe_2O_3 during synthesis. Conversely, the high-resolution Fe 2p XPS spectrum of S-FeP/Fe_2P reveals four doublets at 706.6/719.1, 710.1/723.1, 711.7/725.0, and 715.4/729.9 eV, which corresponded to the Fe–P bonding, Fe^{2+}, Fe^{3+}, and satellite features, respectively [39]. The P 2p high-resolution XPS spectrum (Figure 3B) displays two characteristic peaks at 129.1 eV (P $2p_{3/2}$) and 129.8 eV (P $2p_{1/2}$), originating from Fe–P bonds within the metal phosphide structure [40]. An additional

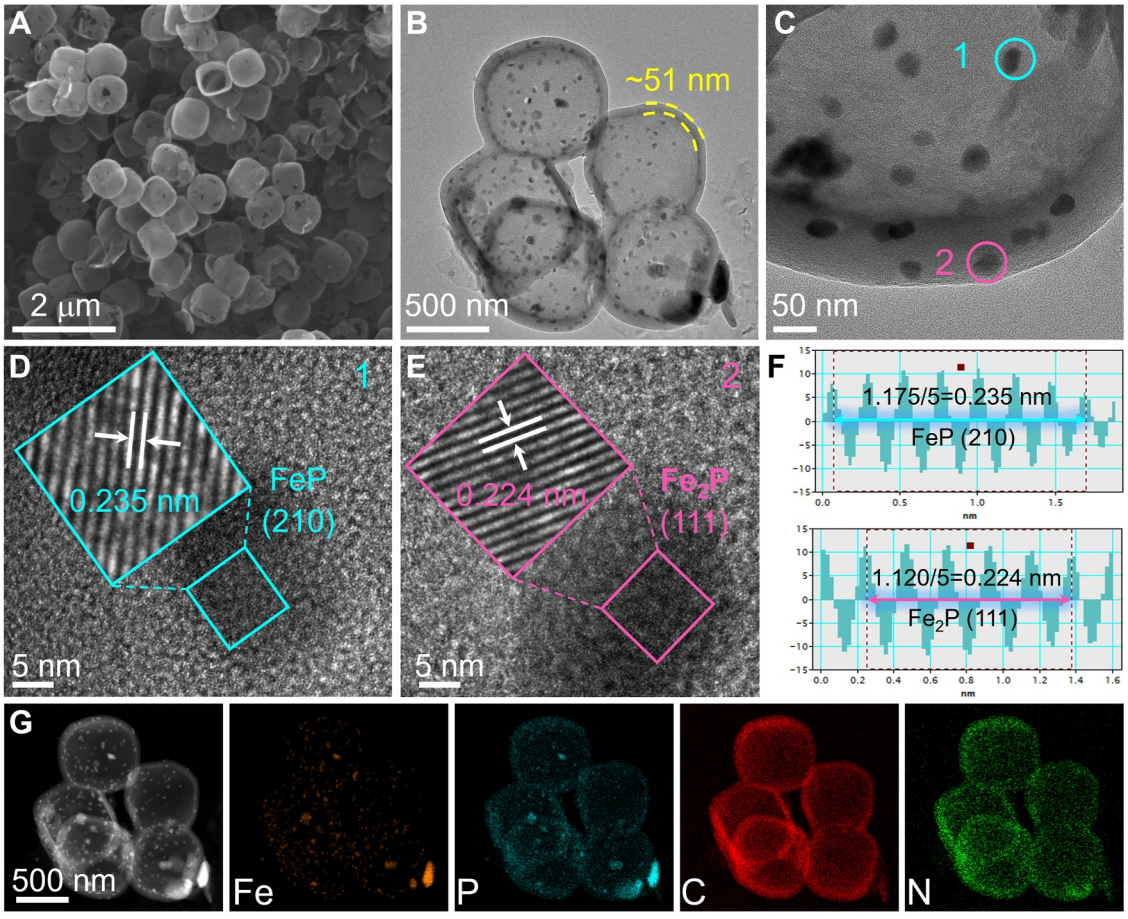

FIGURE 2 | Morphology characterization of as-prepared catalysts. (A) SEM image, (B) TEM image, (C)–(E) HR-TEM images, (F) the lattice spacing profiles of the blue and pink line regions. (G) HAADF-STEM images and the corresponding elemental mappings of H-FeP/Fe_2P.

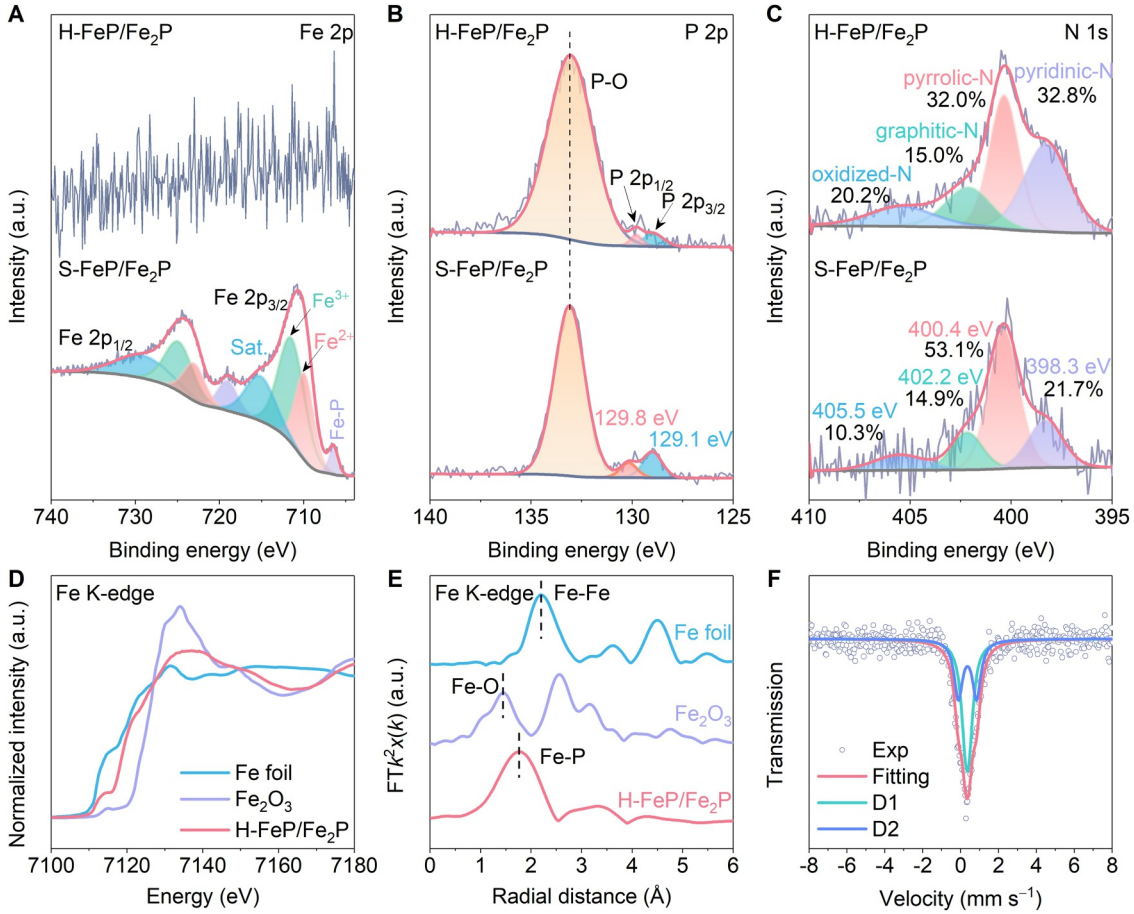

FIGURE 3 | Chemical composition and electronic structure characterization of as-prepared catalysts. High-resolution XPS spectra of (A) Fe 2p, (B) P 2p, and (C) N 1s in as-synthesized samples. (D) Fe K-edge XANES. (E) Fe K-edge FT-EXAFS spectra. (F) The ^{57}Fe Mössbauer spectrum measured at 298 K. Exp., experiment of H-FeP/Fe_2P.

peak at 133.1 eV is attributed to surface P-O bonding, likely a consequence of oxidation during synthesis or air exposure [41]. In addition, the high-resolution N 1s XPS spectra (Figure 3C) show four deconvolution peaks with binding energies of 398.3, 400.4, 402.2, and 405.5 eV corresponding to pyridinic-N, pyrrolic-N, graphitic-N, and oxidized-N, respectively [42]. The XPS spectra for the control samples are illustrated in Supporting Information S1: Figure S11. The N contents in H-FeP/Fe_2P and S-FeP/Fe_2P were investigated based on XPS analysis. The results showed that the graphitic-N content was similar in both samples, whereas the pyridine-N content in H-FeP/Fe_2P was 32.8%, which was higher than that in S-FeP/Fe_2P (21.7%). Notably, pyridine-N plays a pivotal role in ORR by promoting reactant adsorption, whereas graphitic-N substantially enhances catalyst durability and conductivity [43]. These findings suggest that the higher pyridine-N content in H-FeP/Fe_2P may contribute to its superior ORR performance. To confirm the existence of the Fe–P bond, we performed X-ray absorption near edge structure (XANES) and Fourier transform extended X-ray absorption fine structure (FT-EXAFS) of H-FeP/Fe_2P. As shown in Figure 3D, the absorption edge of H-FeP/Fe_2P lies between Fe foil and Fe_2O_3, indicating that the valence state of Fe in H-FeP/Fe_2P is between 0 and +3. In addition, the FT-EXAFS spectrum (Figure 3E) exhibits the most pronounced intensity of the Fe–P oscillatory peak at 1.7 Å, indicating that the Fe–P bond is the nearest-neighbor coordination, which contributes the most to the total spectrum, thus confirming the existence of the Fe–P coordination [24]. Furthermore, the Fourier transform (FT) k^3-weighted EXAFS spectra of the Fe foil and H-FeP-Fe_2P catalyst were analyzed to elucidate their Fe coordination configurations. As displayed in Supporting Information S1: Figure S12, the FT-EXAFS spectrum of the Fe foil exhibits a main peak at 2.2 Å, which is attributed to the Fe–Fe bond [44], whereas the FT-EXAFS spectrum of the H-FeP-Fe_2P catalyst displays a primary peak at 1.76 Å, which is ascribed to the Fe–P bond [45]. The corresponding experimental K-edge FT-EXAFS spectra are presented in Supporting Information S1: Figure S13. The EXAFS fitting results indicate that the first-shell Fe coordination number in the H-FeP-Fe_2P sample is around 2.5 (Supporting Information S1: Table S2), which strongly confirms the co-coordination structure between Fe and P atoms in the H-FeP-Fe_2P catalyst. We performed Mössbauer spectroscopy of H-FeP/Fe_2P (Figure 3F), which revealed two doublets (D1 and D2) attributed to Fe-I (pyramidal sites) and Fe-II (tetrahedral sites) in the FeP/Fe_2P crystal structure [44], which is clearly identified as a high-spin Fe^{3+} site and a low-spin Fe^{2+} site, respectively [46].

The electrocatalytic oxygen reduction reaction (ORR) activity of all catalysts is rated in an oxygen-saturated 0.1 M KOH solution.

As illustrated in Supporting Information S1: Figures S14–S16, an initial assessment of the ORR performance of the synthesized catalysts was performed after the etching of the Fe_2O_3@PDA precursor with HCl for varying durations, adjusting the ratio of precursor to red phosphorus, and optimizing the phosphating temperature. The results indicated that catalytic performance peaked with 24 h of etching, a precursor to red phosphorus ratio of 1:2, and a temperature of 900°C. By comparing the cyclic voltammetry curves in O_2- and N_2-saturated electrolytes (Figure 4A), H-FeP/Fe_2P showed a distinct reduction peak in O_2-saturated condition, confirming the catalytic activity toward ORR [47]. As ORR polarization curves shown in Figure 4B, H-FeP/Fe_2P exhibited the optimal ORR performance with a half-wave potential ($E_{1/2}$) of 0.82 V (vs. RHE), significantly exceed S-FeP/Fe_2P (0.78 V), and was slightly lower than that of Pt/C (0.86 V). Moreover, H-FeP/Fe_2P displays enhanced mass transport and reaction kinetics, as evidenced by its substantially higher limiting current density (J_L = 5.5 mA cm^{-2}) than that of S-FeP/Fe_2P (J_L = 3.2 mA cm^{-2}) and Pt/C (J_L = 5.0 mA cm^{-2}) (Figure 4C). Additionally, the kinetic current density (J_K) was significantly greater than that of the control sample S-FeP/Fe_2P. The superior performance of H-FeP/Fe_2P was also proved by its lower Tafel slope (39 mV dec^{-1}) than those of H-FeP/Fe_2P (127 mV dec^{-1}), and Pt/C (80 mV dec^{-1}), as depicted in Figure 4D. This result demonstrates its exceptional kinetic performance in the ORR process [48]. Moreover, the control catalyst Fe and P samples both exhibited undesirable ORR performance, as illustrated in Supporting Information S1: Figure S17 and Table S3. Significantly, the performance of the proposed H-FeP/Fe_2P also compares favorably with other recently reported Fe-based phosphide catalysts (Figure 4E and Supporting Information S1: Table S4). In addition, LSV curves were recorded at different rotational speeds (400–2025 rpm) to elucidate the optimal ORR pathway for H-FeP/Fe_2P (Figure 4F). The results demonstrated that the J_L gradually increased with the increase of rotational speed. The inset of Figure 4F presents the corresponding linear fit of the Koutecky–Levich (K-L) plot, signifying that H-FeP/Fe_2P exhibits a first-order kinetic response to dissolved oxygen concentration [49, 50]. The electron transfer number estimated by the K-L equation was approximately 4, suggesting an effective four-electron transfer pathway [51, 52]. In addition, rotating ring disc electrode tests were performed (Figure 4G). In addition, the electron transfer number is close to the four-electron (n = 3.9), revealing that 4e^- reaction process and high selectivity on H-FeP/Fe_2P. The electrochemically active surface area (ECSA) was evaluated via the double-layer capacitance (C_{dl}) at varying scan rates (10–35 mV s^{-1}), as shown in Supporting Information S1: Figure S18. As depicted in Figure 4H, the ECSA of H-FeP/Fe_2P markedly exceeds that of S-FeP/Fe_2P, attributed to the hollow structure

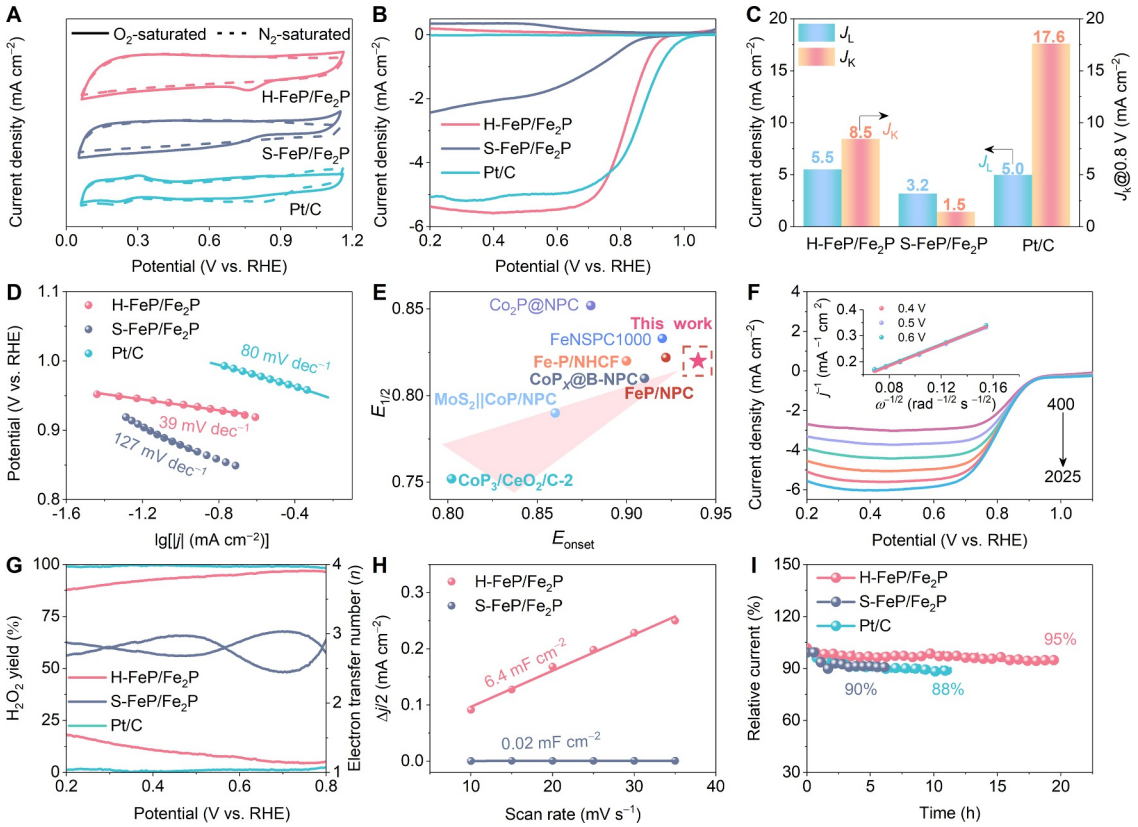

FIGURE 4 | Electrochemical performance of as-prepared catalysts. (A) Cyclic voltammetry (CV) curves in N_2 or O_2-saturated 0.1 M KOH solution. (B) Linear sweep voltammetry (LSV) polarization curves in O_2-saturated 0.1 M KOH electrolyte, (C) the corresponding limiting current density (J_L) and kinetic current density (J_K), (D) Tafel plots. (E) Comparison of the ORR activity of H-FeP/Fe_2P with recently reported electrocatalysts. (F) Polarization curves of H-FeP/Fe_2P with various rotating speeds from 400 to 2025 rpm (inset: the corresponding Koutecky–Levich (K-L) plots). (G) H_2O_2 yield (%) and electron transfer number (n), (H) double layer capacitance (C_{dl}) values from different catalysts. (I) The corresponding stability test in O_2-saturated 0.1 M KOH solution at a rotating speed of 1600 rpm.

that enhances the accessibility of active sites [53, 54]. The durability of electrocatalyst is widely acknowledged as significant hurdles for large-scale application. In a continuous 20 h test, H-FeP/Fe_2P demonstrated remarkable stability, achieving a current retention of 95%. In contrast, S-FeP/Fe_2P maintained only 90% retention over 6 h, whereas Pt/C exhibited 88% retention after 11 h (Figure 4I). In addition, CV measurements using $K_3[Fe(CN)_6]$ were performed to evaluate the ECSA of the synthesized catalysts (Supporting Information S1: Figure S19). As anticipated, the results revealed that H-FeP/Fe_2P exhibited the largest slope in contrast to S-FeP/Fe_2P (Supporting Information S1: Figure S20), attributed to the hollow structure exposing more active sites [55]. Thiocyanate anions (SCN^-) were employed as probes to distinguish active centers due to their propensity to form complexes with a range of metals (e.g., Fe and Co) [56, 57]. In H-FeP/Fe_2P, the Fe–P species are predominantly encapsulated within the CN armor, which effectively safeguards the active sites from the toxicity of SCN^- and inhibits interactions with the oxygen feedstock [58]. Consequently, upon the introduction of SCN^- ions, H-FeP/Fe_2P displayed only minimal deactivation, with $E_{1/2}$ decreasing by merely 0.05 V (Supporting Information S1: Figure S21). This observation suggests that the Fe species acts as the critical active center for catalytic performance, whereas the armor provides a protective function. During the *i*–*t* chronoamperometric test, the methanol crossover effect was evaluated through the immediate injection of methanol into an O_2-saturated 0.1 M KOH solution. As illustrated in Supporting Information S1: Figure S22, at 420 s post-injection, the current of H-FeP/Fe_2P remained nearly undisturbed, whereas the current for Pt/C experienced a sharp decline. This result underscores the exceptional methanol resistance of H-FeP/Fe_2P, indicating its promising potential as a high-performance catalyst for direct methanol fuel cells [59]. SEM analysis was performed after the stability tests on the H-FeP/Fe_2P catalyst. The results indicated that it preserved its original hollow structure, with only negligible agglomeration observed (Supporting Information S1: Figure S23), providing robust evidence of its structural stability.

To elucidate the reaction pathways and mechanisms of the catalyst, in situ Raman spectroscopy (device shown in Figure 5A) and in situ Fourier transform infrared (FTIR) spectroscopy were utilized to monitor the active sites and key reactions at varying potentials. During the alkaline ORR process, as the applied potential decreased, characteristic vibrational peaks corresponding to $^*O_2^-$ and *OOH emerged at 1161 and 1507 cm^{-1}, respectively (Figure 5B and Supporting Information S1: Figure S24a) [60]. Notably, these two peaks appeared at a lower potential (0.8 V) for H-FeP/Fe_2P compared to S-FeP/Fe_2P, which commenced around 0.6 V. This observation indicates that the hollow structure of H-FeP/Fe_2P is more favorable for the initial activation of O_2 and subsequent formation of intermediates. In-situ FTIR analysis,

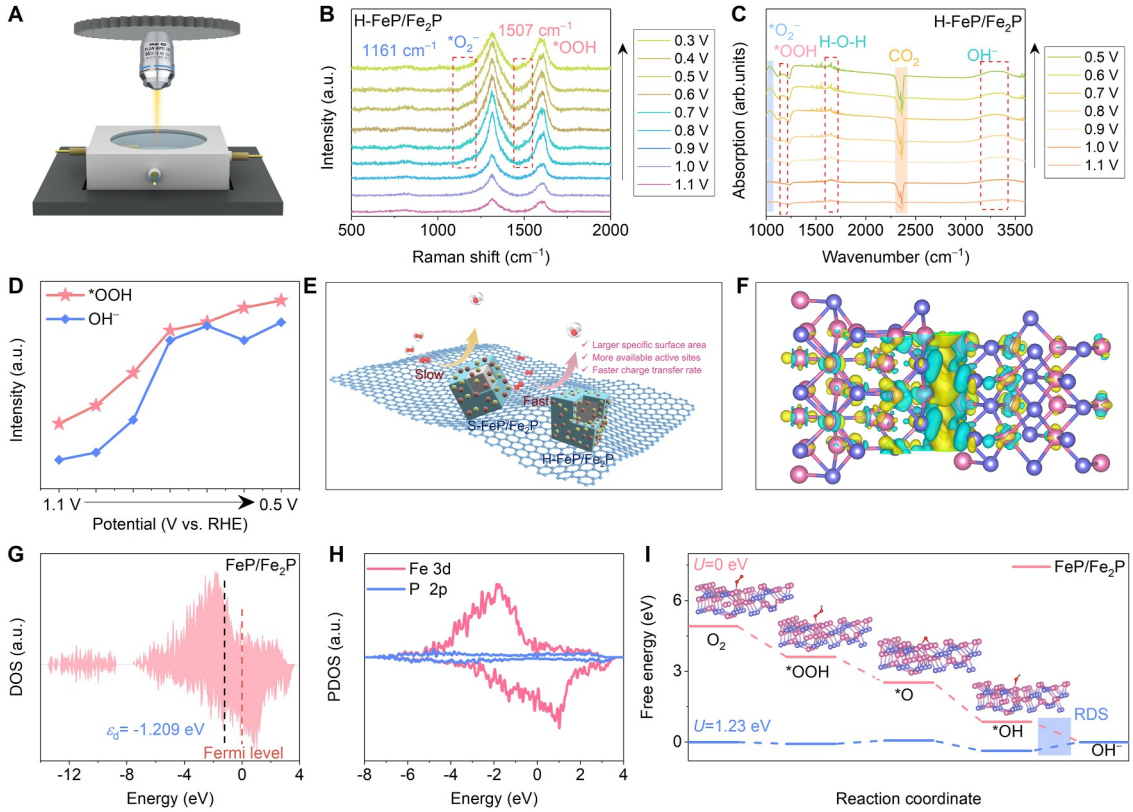

FIGURE 5 | Electrocatalytic mechanism of as-prepared catalysts. (A) Schematic diagram of the in situ Raman electrolyzer. (B) In situ Raman spectra of H-FeP/Fe_2P, (C) in situ FTIR spectra of H-FeP/Fe_2P. (D) Normalized intensity analysis of the characteristic vibrational peaks of *OOH and OH^- in in-situ FTIR spectra of H-FeP/Fe_2P catalyst. (E) Diagram showing the advantages of H-FeP/Fe_2P toward ORR. (F) Differential charge density, the yellow and green regions represent electron accumulation and depletion, respectively (pink represents the Fe element and purple represents the P element). (G) The DOS plots, (H) PDOS of Fe d-state and P p-state, (I) Gibbs free energy profile of ORR (the insets are ORR mechanism on H-FeP/Fe_2P).

the peak observed at 1640 cm^{-1} was attributed to H–O–H vibration, whereas the band at 3310 cm^{-1} corresponded to OH^- species. The increase in intensity of the OH^- peak signifies continuous accumulation of products, reflecting ongoing ORR activity [61]. As the potential diminished, the peaks at 1239 and 1159^{-1} were assigned to adsorbed $^*OOH$ intermediates on the catalyst surface [62]. Additionally, a peak at 1050 cm^{-1} was associated with O–O stretching modes ($*O_2^-$) within adsorbed O_2 molecules (Figure 5C and Supporting Information S1: Figure S24b) [61]. These findings suggest that H-FeP/Fe_2P exhibits robust catalytic capability for converting O_2 into $^*OOH$ [63], whereas S-FeP/Fe_2P displays relatively weak signals for $^*O_2^-$ species. This disparity may be attributed to its hollow structure, which facilitates greater exposure of active sites for adsorbing O_2 molecules, thus enhancing the coverage of the $^*OOH$ intermediate on the catalyst surface, consistent with the in situ Raman results. In Figure 5D, the intensities of $^*OOH$ and OH^- vibrational bands on H-FeP/Fe_2P increase significantly with decreasing applied potential, validating effective ORR activity. As illustrated in Figure 5E, it is evident that the hollow structure obtained through acid etching possesses a unique advantage in promoting ORR activity.

To explore the exceptional ORR performance of the synthesized catalyst, we performed density functional theory (DFT) calculations. Based on the exposed crystal planes identified from HR-TEM imaging, we modeled extended surfaces oriented along the (210) direction for FeP and the (111) direction for Fe_2P. The charge density distribution on FeP/Fe_2P is shown in Figure 5F, where the cyan region indicates electron depletion and the yellow region indicates electron accumulation. It can be clearly seen that electrons accumulate around the Fe atoms, whereas the P atoms act as electron-withdrawal sites. To analyze electronic structure of the catalyst, we calculated its density of states (DOS) and d-band center (ε_d). The DOS of the catalyst exceeds the Fermi energy level (E-E_f = 0) with overlapping conduction and valence bands, consistent with typical metallic behavior (Figure 5G). The projected density of states (PDOS) analysis (Figure 5H) reveals a marked dominance of Fe d-orbital states over P p-orbital states near the Fermi level, demonstrating superior electron density localization in Fe. This electronic configuration directly correlates with improved conductivity and enhanced ORR performance [64, 65]. Figure 5I delineates the ORR pathway and rate-determining step (RDS) under alkaline conditions (U = 0 V), revealing the whole ORR process to be thermodynamically spontaneous, with the fourth step identified as the RDS. Notably, the ΔG_{RDS} of FeP/Fe_2P is −0.37 eV at U = 1.23 V, which is significantly lower than that of Pt/C (0.61 eV) [66]. This indicates that the reaction kinetics of FeP/Fe_2P is superior to that of Pt/C [67].

In light of the superior electrocatalytic performance of H-FeP/Fe_2P, zinc-air batteries (ZABs) were assembled to assess their promising applications in energy storage and conversion systems. A schematic illustration of the assembled ZAB is shown in Figure 6A, featuring a polished zinc anode, a catalyst-coated carbon cloth air cathode, and a 6.0 M KOH electrolyte containing 0.2 M $Zn(AC)_2$. The open-circuit voltage of H-FeP/Fe_2P-based ZAB was 1.52 V, surpassing that the 1.27 V of S-FeP/Fe_2P and 1.49 V of Pt/C (Figure 6B). Remarkably, H-FeP/Fe_2P also exhibited an ultra-high power density of 175 mW cm^{-2} compared to the 128 mW cm^{-2} of Pt/C (Figure 6C), indicating a higher

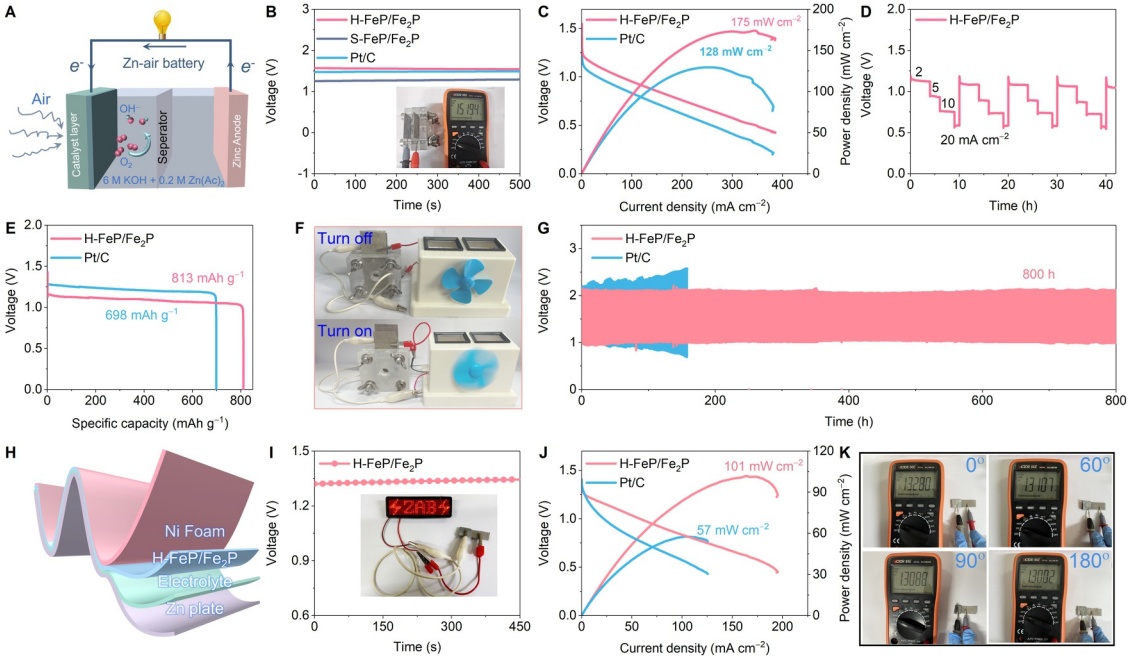

FIGURE 6 | Performance of assembled aqueous and flexible ZAB (FZAB). (A) Schematic configuration of assembled aqueous ZAB. (B) OCV of the ZABs (inset: an optical image for OCV measured by a multimeter). (C) Discharge polarization curves and the corresponding power densities of the ZABs. (D) Discharge curves at various current densities (2–20 mA cm^{-2}). (E) Specific capacity plots. (F) Photos of toy fan powered by H-FeP/Fe_2P-based ZAB. (G) Galvanostatic cycling at 5 mA cm^{-2} (20 min for each cycle). (H) Sketch diagram of the FZAB. (I) OCVs of H-FeP/Fe_2P and Pt/C-based FZABs (inset: H-FeP/Fe_2P-based FZAB-lit LED panel). (J) The discharge polarization and corresponding power density profiles of the FZABs. (K) OCVs at different bending angles of H-FeP/Fe_2P-based flexible ZAB.

activity. Figure 6D shows the discharge rate performance of ZAB at different current densities. It was observed that as the current density was elevated from 2 to 20 mA cm^{-2}, the discharge voltage concomitantly decreased. Remarkably, after four cycles, when the current density was reverted to the initial value of 2 mA cm^{-2}, the discharge voltage exhibited a remarkably minimal decrease of merely 0.06 V, highlighting the exceptional cycling stability of the ZAB. Furthermore, it achieved a specific capacity of 813 mAh g^{-1}_{Zn}, exceeding Pt/C (698 mAh g^{-1}_{Zn}) under the same operating conditions (Figure 6E). In practice, the ZAB integrated with H-FeP/Fe_2P successfully powered a toy fan (Figure 6F), validating its prospective utility for energy storage and conversion applications. As H-FeP/Fe_2P delivers an oxygen evolution reaction (OER) overpotential of 403 mV at 10 mA cm^{-2} (Supporting Information S1: Figure S25), its activity is insufficient to support practical application. Accordingly, a 1:1 composite of H-FeP/Fe_2P and RuO_2 was assembled as the air cathode to evaluate extended charge–discharge cycling, with a Pt/C + RuO_2 benchmark prepared in concert for rigorous comparison. The long-term rechargeability of the ZABs were appraised by continuous galvanostatic charging/discharging at a current density of 5 mA cm^{-2} for 20 min per cycle. The H-FeP/Fe_2P-based ZAB can operate stably for more than 800 h continuously without any pronounced degradation in performance, whereas the Pt/C + RuO_2-based ZAB suffered from serious decay after merely 160 h (Figure 6G). Moreover, the H-FeP/Fe_2P-based ZAB significantly outperforms previously reported most transition metal phosphide-based ZABs across all performance metrics (Supporting Information S1: Table S3). Flexible zinc-air batteries (FZABs) offer high energy density, inherent safety, and flexibility, making them ideal for powering flexible electronics. As illustrated in Figure 6H, FZABs were fabricated by employing catalyst-coated carbon cloth (CC) as the air cathode, zinc foil as the anode, and polyvinyl alcohol (PVA) hydrogel as the solid electrolyte. The H-FeP/Fe_2P-based FZAB yielded a stable open-circuit voltage of 1.33 V (Figure 6I), and sufficient power to illuminate a red LED (inset in Figure 6I). As depicted in Figure 6J, the assembled-FZAB achieved a peak power density of 101 mW cm^{-2}, which is better than that of Pt/C (57 mW cm^{-2}) and other transition metal phosphide based FZABs (Supporting Information S1: Table S4). In addition, the constructed FZAB maintained stable voltage under different bending states (0°, 60°, 90°, and 180°), demonstrating its robust mechanical flexibility (Figure 6K). The superior ZAB properties of H-FeP/Fe_2P underscore its potential for enhanced energy storage and conversion applications.

4 | Conclusions

In summary, a hollow FeP/Fe_2P catalyst with graphite shell layer protection was successfully constructed by acid etching of dopamine-coated Fe_2O_3 precursor and combined with high-temperature phosphatization, which exhibited excellent ORR performance. The hollow graphite shell layer structure effectively inhibited the migration, aggregation and dissolution of phosphides while maximally retaining the accessibility of active sites. In situ characterization techniques and theoretical calculations reveal that adsorbed $^*OH$ can accelerate the kinetics of the ORR reaction via facilitating the dissociation of the oxygen-oxygen bond on the iron active site. H-FeP/Fe_2P catalyst achieves a limiting current density of 5.5 mA cm^{-2} and a kinetic current density of 8.5 mA cm^{-2}, outperforming commercial Pt/C catalysts (J_L = 4.7 mA cm^{-2}, J_K = 5.7 mA cm^{-2}). The zinc-air battery assembled with this catalyst achieved a cycle stability of more than 800 h and a high specific capacity of 813 mAh g^{-1}_{Zn}, ranking among the top-performing transition metal phosphide-based systems reported to date. In addition, the solid-state zinc-air batteries incorporating H-FeP/Fe_2P cathode demonstrated excellent reliability, flexibility and durability under various deformation conditions, providing a new paradigm for flexible electronic power supplies. This work not only provides a novel design strategy for high-performance transition metal phosphide catalysts but also lays a significant foundation for developing liquid/flexible zinc-air batteries with enhanced activity and long-term stability.

Author Contributions

Li-Xia Wang: investigation, writing – original draft. **Jia-Sui Huang:** investigation. **Xiao-Yang Cheng:** data curation. **Zhi-Yang Huang:** data curation. **A-Lin Zhou:** data curation. **Shu-Hui Sun:** supervision, writing – review and editing. **Xiu-Lin Yang:** supervision, writing – review and editing. **Tian-Xiao Sun:** supervision, writing – review and editing. **Bin Wu:** conceptualization, supervision, writing – review and editing.

Acknowledgments

This study was financially supported by the National Natural Science Foundation of China (Grant Nos. 21965005 and 52363028), the Natural Science Foundation of Guangxi Province (Grant No. 2021GXNSFA076001), Guangxi Technology Base and Talent Subject (Grant Nos. GUIKE AD18126001, GUIKE AD20297039), the Innovation Project of Guangxi Graduate Education (Grant No. YCBZ2023056), the National Research Foundation, Singapore, and A*STAR (Agency for Science, Technology and Research) under its LCER Phase 2 Programme 1st Emerging Technology (Award No. U2411D4006), and the Key Laboratory of Functional Inorganic Material Chemistry (Heilongjiang University), Ministry of Education, P. R. China.

Conflicts of Interest

The authors declare no conflicts of interest.

Data Availability Statement

The data that support the findings of this study are available from the corresponding author upon reasonable request.

References

1. J. Luo, Y. Zhang, Z. Lu, et al., "Oxygen-Coordinated Cr Single-Atom Catalyst for Oxygen Reduction Reaction in Proton Exchange Membrane Fuel Cells," *Angewandte Chemie International Edition* 64, no. 9 (2025): e202500500, https://doi.org/10.1002/anie.202500500.

2. Y. Sun, L. Wang, H. Li, et al., "N-, S-Codoped Porous Carbon With Trace Single-Atom Fe for Enhanced Oxygen Reduction With Robust Poison Resistance and Efficient Rechargeable Zinc–Air Battery," *Carbon Neutralization* 4, no. 2 (2025): e196, https://doi.org/10.1002/cnl2.196.

3. S. Surendran, Y. Lim, S. Lee, et al., "Understanding the Engineering Tactics to Achieve the Stabilized Anode in Next-Generation Zn-Air Batteries," *Exploration* 5, no. 3 (2025): 20240054, https://doi.org/10.1002/EXP.20240054.

4. Y. Zhang, J.-Y. Song, J.-D. Hu, L.-F. Liu, C.-M. Zhang, and J.-S. Li, "Salt Template Synthesis of Coo@Co Nanoparticles Encapsulated in 3D Porous Nitrogen-Doped Carbon for Oxygen Reduction Reaction," *cMat* 1, no. 3 (2024): e32, https://doi.org/10.1002/cmt2.32.

5. W.-B. Tu, L.-N. Song, S. Liang, et al., "Designing Hydrophobic Micro-Three-Phase Reaction Interfaces to Enhance the ORR Kinetics Toward Zinc-Air Battery," *Advanced Energy Materials* 15, no. 8 (2025): 2404946, https://doi.org/10.1002/aenm.202404946.

6. L. Zhang, M.-L. Li, S.-S. Gao, et al., "Group VIII Elements-Based Single-Atom Electrocatalysts for Energy Conversion: A Mini Review," *Rare Metals* 44, no. 7 (2025): 4532–4550, https://doi.org/10.1007/s12598-025-03260-8.

7. Y.-M. Zhang, Z.-R. Zhou, L.-L. Zhao, et al., "Homologous Heterostructure of MoS_2 and MoO_2 Coupled With Carbon Layers as Cathode Catalyst for Rechargeable Lithium–Oxygen Batteries," *Rare Metals* 43, no. 7 (2024): 3383–3390, https://doi.org/10.1007/s12598-024-02683-z.

8. Q. Liu, J. Qin, F. Huang, D. Zhang, L. Chen, and F. Yin, "Dysprosium Regulated Platinum Particles as a Bimetallic Alloy Catalyst for Oxygen Reduction Reaction," *Journal of Rare Earths* 41, no. 8 (2023): 1189–1194, https://doi.org/10.1016/j.jre.2022.08.017.

9. J. Long, K.-W. Zhuang, W. Liao, et al., "Electronegativity-Assisted Optimized Electronic Structure of Functionalized-Pt Catalysts for Boosting Oxygen Reduction Kinetics," *Rare Metals* 43, no. 5 (2024): 1965–1976, https://doi.org/10.1007/s12598-023-02580-x.

10. X.-G. Wu, R. Wang, F. Ma, et al., "FeCo-N Encapsuled in Nitrogen-Doped Carbon Nanotubes as Bifunctional Electrocatalysts With a High Stability for Zinc Air Batteries," *Rare Metals* 42, no. 5 (2023): 1526–1534, https://doi.org/10.1007/s12598-022-02173-0.

11. C.-X. Xu, J.-J. Zhang, H.-R. Dou, et al., "Fe_4N Particles Embedded in Nitrogen-Doped Electrospun Carbon Nanofibers as Efficient ORR Catalysts for Zinc-Air Battery," *Rare Metals* 44, no. 5 (2025): 3156–3169, https://doi.org/10.1007/s12598-024-03167-w.

12. Y.-T. Zhang, F. Zhang, Z. Lu, et al., "CrN Supported by Carbon Nanosheets as Efficient Catalysts Toward Oxygen Reduction Reaction and Zn-Air Batteries," *Rare Metals* 43, no. 10 (2024): 4973–4981, https://doi.org/10.1007/s12598-024-02855-x.

13. D. Deng, W. Zhang, J. Qian, et al., "Charge Delocalization Regulation of Atomically Dispersed Tungsten Sites by Axial Sulfur Atoms for Highly Active Oxygen Reactions in Low-Temperature Zinc-Air Batteries," *Nano Energy* 134 (2025): 110579, https://doi.org/10.1016/j.nanoen.2024.110579.

14. D. Deng, H. Ma, S. Wu, et al., "Engineering Electronic Density and Coordination Environment of Mn-N_x Sites via Zn Cooperation for Quasi-Solid-State Zinc-Air Batteries," *Renewables* 1, no. 3 (2023): 362–372, https://doi.org/10.31635/renewables.023.202200020.

15. W. Deng, Z. Song, M. Jing, T. Wu, W. Li, and G. Zou, "Highly Active Air Electrode Catalysts for Zn-Air Batteries: Catalytic Mechanism and Active Center From Obfuscation to Clearness," *Carbon Neutralization* 3, no. 4 (2024): 501–532, https://doi.org/10.1002/cnl2.133.

16. X.-L. Hu, J.-C. Fan, X. Li, Z.-K. Wu, Y.-Y. Li, and C.-H. Xu, "Interfaces Engineering of Heterostructured NiCoP/NiFe LDH@CC for Attaining High Catalytic Activity in Long-Lasting Rechargeable Zn–Air Batteries," *Rare Metals* 43, no. 10 (2024): 4961–4972, https://doi.org/10.1007/s12598-024-02748-z.

17. S.-Q. Li, K. Sun, Y.-Y. Liu, et al., "Coupling Co_2P Nanoparticles Onto N,P-Doped Biomass-Derived Carbon as Efficient Electrocatalysts for Flexible Zn–Air Batteries," *Rare Metals* 43, no. 10 (2024): 4982–4991, https://doi.org/10.1007/s12598-024-02829-z.

18. K. Chen, L. Wang, J. Long, F. Zhao, and L. Kang, "Petaloid CoP/FeP Composites: Efficiently Bifunctional Cathode Electrochemical Oxygen Catalysts for Aqueous and Solid-State Zinc-Air Batteries," *Chemical Engineering Journal* 496, no. 15 (2024): 153820, https://doi.org/10.1016/j.cej.2024.153820.

19. M. Du, D. Li, S. Liu, and J. Yan, "Transition Metal Phosphides: A Wonder Catalyst for Electrocatalytic Hydrogen Production," *Chinese Chemical Letters* 34, no. 9 (2023): 108156, https://doi.org/10.1016/j.cclet.2023.108156.

20. W. Liu, H. Gao, Z. Zhang, et al., "CoP/Cu_3P Heterostructured Nanoplates for High-Rate Supercapacitor Electrodes," *Chemical Engineering Journal* 437, no. 1 (2022): 135352, https://doi.org/10.1016/j.cej.2022.135352.

21. X. Yang, F. Wang, Z. Jing, et al., "A General 'In Situ Etch-Adsorption-Phosphatization' Strategy for the Fabrication of Metal Phosphides/Hollow Carbon Composite for High Performance Liquid/Flexible Zn–Air Batteries," *Small* 19, no. 38 (2023): 2301985, https://doi.org/10.1002/smll.202301985.

22. M. Tahir, M. A. Farid, E. Aliyev, Z. Huang, J.-J. Zou, and S. Du, "Cobalt Phosphide Decorating Metallic Cobalt With a Nitrogen-Doped Carbon Nano-Shell Surpasses Platinum Group Metals for Oxygen Electrocatalysis Applications," *Battery Energy* 3, no. 6 (2024): 20240029, https://doi.org/10.1002/bte2.20240029.

23. J. Kundu, T. Kwon, K. Lee, and S.-I. Choi, "Exploration of Metal-Free 2D Electrocatalysts Toward the Oxygen Electroreduction," *Exploration* 4, no. 4 (2024): 20220174, https://doi.org/10.1002/EXP.20220174.

24. L. Chen, Y. Zhang, L. Dong, et al., "Honeycomb-Like 3D N-, P-Codoped Porous Carbon Anchored With Ultrasmall Fe_2P Nanocrystals for Efficient Zn-Air Battery," *Carbon* 158 (2020): 885–892, https://doi.org/10.1016/j.carbon.2019.11.073.

25. Y. Tang, J. Ding, W. Zhou, et al., "Design of Uniform Hollow Carbon Nanoarchitectures: Different Capacitive Deionization Between the Hollow Shell Thickness and Cavity Size," *Advanced Science* 10, no. 9 (2023): 2206960, https://doi.org/10.1002/advs.202206960.

26. J. M. Yoo, H. Shin, D. Y. Chung, and Y.-E. Sung, "Carbon Shell on Active Nanocatalyst for Stable Electrocatalysis," *Accounts of Chemical Research* 55, no. 9 (2022): 1278–1289, https://doi.org/10.1021/acs.accounts.1c00727.

27. M. Tadic, D. Trpkov, L. Kopanja, S. Vojnovic, and M. Panjan, "Hydrothermal Synthesis of Hematite (α-Fe_2O_3) Nanoparticle Forms: Synthesis Conditions, Structure, Particle Shape Analysis, Cytotoxicity and Magnetic Properties," *Journal of Alloys and Compounds* 792 (2019): 599–609, https://doi.org/10.1016/j.jallcom.2019.03.414.

28. M. Safari, J. Mazloom, K. Boustani, and A. Monemdjou, "Hierarchical Fe_2O_3 Hexagonal Nanoplatelets Anchored on SnO_2 Nanofibers for High-Performance Asymmetric Supercapacitor Device," *Scientific Reports* 12, no. 1 (2022): 14919, https://doi.org/10.1038/s41598-022-18840-2.

29. L.-H. Xu, P.-C. Che, X.-J. Zhang, S. Cosnier, and D. Shan, "FeP Nanoparticles Highly Dispersed on N,P-Doped Petaloid Carbon Nanosheet: Interface Engineering and Boosted Intrinsic ORR Activity," *Applied Surface Science* 620 (2023): 156770, https://doi.org/10.1016/j.apsusc.2023.156770.

30. J. Zou, M. Zheng, H. Wu, et al., "FeP/Fe_2P Heterojunction Embedded in N, S, P-Doped Carbon Structure as Oxygen Reduction Reaction Electrocatalysts for Zinc-Air Batteries," *Journal of Energy Storage* 70 (2023): 107950, https://doi.org/10.1016/j.est.2023.107950.

31. S. Wang, P. Yang, X. Sun, et al., "Synthesis of 3D Heterostructure Co-Doped Fe_2P Electrocatalyst for Overall Seawater Electrolysis," *Applied Catalysis B: Environment and Energy* 297 (2021): 120386, https://doi.org/10.1016/j.apcatb.2021.120386.

32. J. Xie, S. Wu, C. Luo, et al., "Modulating Electronic Structure of Active Sites on Iron-Based Nanoparticles Enhances Peroxymonosulfate Activation," *Applied Catalysis B: Environment and Energy* 354 (2024): 124138, https://doi.org/10.1016/j.apcatb.2024.124138.

33. J. Rong, G. Zhu, W. Ryan Osterloh, et al., "In Situ Construction MoS_2-Pt Nanosheets on 3D MOF-Derived S, N-doped Carbon Substrate for Highly Efficient Alkaline Hydrogen Evolution Reaction," *Chemical*

Engineering Journal 412 (2021): 127556, https://doi.org/10.1016/j.cej.2020.127556.

34. X. Zhang, Z. Zhao, J. Xu, et al., "N-Doped Carbon Nanotube Arrays on Reduced Graphene Oxide as Multifunctional Materials for Energy Devices and Absorption of Electromagnetic Wave," *Carbon* 177 (2021): 216–225, https://doi.org/10.1016/j.carbon.2021.02.085.

35. H. Luo, J. Wang, S. Zhang, et al., "In Situ Symbiosis of Cerium Oxide Nanophase for Enhancing the Oxygen Electrocatalysis Performance of Single-Atom Fe-N-C Catalyst With Prolonged Stability for Zinc–Air Batteries," *Small* 20, no. 38 (2024): 2400357, https://doi.org/10.1002/smll.202400357.

36. C. Xu, Y. Niu, S. Gong, et al., "Integrating Bimetal Alloy Into N-Doped Carbon Nanotubes@Nanowires Superstructure for Zn-Air Batteries," *ChemSusChem* 15, no. 8 (2022): e202200312, https://doi.org/10.1002/cssc.202200312.

37. T. Li, S. Ren, C. Zhang, et al., "Cobalt Single Atom Anchored on N-Doped Carbon Nanoboxes as Typical Single-Atom Catalysts (SACs) for Boosting the Overall Water Splitting," *Chemical Engineering Journal* 458 (2023): 141435, https://doi.org/10.1016/j.cej.2023.141435.

38. L. Wang, J. Huang, Z. Huang, H. Li, T. Taylor Isimjan, and X. Yang, "Revealing Dynamic Structural Evolution of V and P Co-Doping-Induced Co Defects as Large-Current Water Oxidation Catalyst," *Chemical Engineering Journal* 472, no. 15 (2023): 144924, https://doi.org/10.1016/j.cej.2023.144924.

39. Q. Yu, X. Liu, G. Liu, et al., "Constructing Three-Phase Heterojunction With 1D/3D Hierarchical Structure as Efficient Trifunctional Electrocatalyst in Alkaline Seawater," *Advanced Functional Materials* 32, no. 46 (2022): 2205767, https://doi.org/10.1002/adfm.202205767.

40. W. Li, X. Liu, X. Li, et al., "MoC_x/CoP Janus Structure Embedded Carbon Frame for Boosting Hydrazine Oxidation and Hydrogen Evolution Reactions," *Small* 21, no. 8 (2025): 2500135, https://doi.org/10.1002/smll.202500135.

41. W. Yu, Q. Li, W. Xiao, et al., "Unique CoP Microflower Decorated With Phosphorous-Enriched PtP_2 onto Nickel Foam With Interfacial Electronic Interactions to Boost Alkaline Water-Splitting," *Advanced Functional Materials* 34, no. 27 (2024): 2313935, https://doi.org/10.1002/adfm.202313935.

42. K. Yu, S. Guan, W. Zhang, et al., "Engineering Asymmetric Electronic Structure of Co-N-C Single-Atomic Sites Toward Excellent Electrochemical H_2O_2 Production and Biomass Upgrading," *Angewandte Chemie International Edition* 64, no. 9 (2025): e202502383, https://doi.org/10.1002/anie.202502383.

43. T. Lu, N. Xu, L. Guo, et al., "Constructing 'π-π' Reinforced Bridge Carbon Nanofibers With Highly Active Co-N/C@pyridine N/C@CNTs Sites as Free-Standing Bifunctional Oxygen Electrodes for Zn-Air Batteries," *Advanced Fiber Materials* 6, no. 4 (2024): 1108–1121, https://doi.org/10.1007/s42765-024-00413-9.

44. Y. Pan, X. Ma, M. Wang, et al., "Construction of N, P Co-Doped Carbon Frames Anchored With Fe Single Atoms and Fe_2P Nanoparticles as a Robust Coupling Catalyst for Electrocatalytic Oxygen Reduction," *Advanced Materials* 34, no. 29 (2022): 2203621, https://doi.org/10.1002/adma.202203621.

45. H. Jin, R. Yu, P. Ji, et al., "Sharply Expanding Single-Atomically Dispersed Fe–N Active Sites Through Bidirectional Coordination for Oxygen Reduction," *Chemical Science* 15, no. 19 (2024): 7259–7268, https://doi.org/10.1039/D4SC01329H.

46. A. Han, Z. Zhang, J. Yang, D. Wang, and Y. Li, "Carbon-Supported Single-Atom Catalysts for Formic Acid Oxidation and Oxygen Reduction Reactions," *Small* 17, no. 16 (2021): 2004500, https://doi.org/10.1002/smll.202004500.

47. Z. Li, Y. Yao, Y. Niu, et al., "Multi-Heteroatom-Doped Hollow Carbon Tubes as Robust Electrocatalysts for the Oxygen Reduction Reaction, Oxygen and Hydrogen Evolution Reaction," *Chemical Engineering Journal* 418 (2021): 129321, https://doi.org/10.1016/j.cej.2021.129321.

48. Z. Chen, J. Jiang, M. Jing, et al., "Covalent Organic Framework-Derived Fe, Co-Nitrogen Codoped Carbon as a Bifunctional Electrocatalyst for Rechargeable Efficient Zn–Air Batteries," *Carbon Neutralization* 3, no. 4 (2024): 689–699, https://doi.org/10.1002/cnl2.145.

49. X. Shu, X. Cao, B. He, et al., "Coupling of Indium Clusters With Atomic Fe–N_4 on Carbon for Long-Term Rechargeable Zn–Air Batteries," *Energy & Environmental Science* 18 (2025): 1262–1271, https://doi.org/10.1039/D4EE04465G.

50. Z. Lv, Z. Shu, J. Luo, et al., "Asymmetric High-Coordination Co-NSP Single-Atom Catalysts With Tailored d-p-orbital Electron Structure for Efficient Bifunctional Catalyst of Rechargeable Zn-air Battery Cathodes," *Applied Catalysis B: Environment and Energy* 365 (2025): 124889, https://doi.org/10.1016/j.apcatb.2024.124889.

51. Z. Song, Q. Zhang, Y. Zhang, et al., "Regulating Coordination Environment of Atomic Dimer Catalysts for High Performance Oxygen Reduction Reaction in Fuel Cells," *Applied Catalysis B: Environment and Energy* 365 (2025): 124970, https://doi.org/10.1016/j.apcatb.2024.124970.

52. J. Huang, X. Xu, Y. Yan, et al., "Facile Microwave Synthesis of Kilogram-Scale Electrocatalysts With Nanocarbons Bridged Cobalt Active Sites for Enhanced Oxygen Electrocatalysis," *Advanced Energy Materials* 15, no. 27 (2025): 2500360, https://doi.org/10.1002/aenm.202500360.

53. C. Shi, R. Xu, T. Suo, X. Shi, and R. Yun, "Atomically Dispersed Iron Sites on a Multi-Shelled Hollow Structure for Highly Efficient CO_2 Fixation," *Journal of Materials Chemistry A* 13, no. 8 (2025): 5615–5620, https://doi.org/10.1039/D4TA07903E.

54. Y. Lee, J. H. Lee, D. Lee, et al., "Low-Loading Platinum-Cobalt Electrocatalyst Supported on Hollow Carbon for Enhanced Oxygen Reduction Reaction," *Chemical Engineering Journal* 500 (2024): 157072, https://doi.org/10.1016/j.cej.2024.157072.

55. F. Shahbazi Farahani, M. S. Rahmanifar, A. Noori, et al., "Trilayer Metal–Organic Frameworks as Multifunctional Electrocatalysts for Energy Conversion and Storage Applications," *Journal of the American Chemical Society* 144, no. 8 (2022): 3411–3428, https://doi.org/10.1021/jacs.1c10963.

56. K. Kim, G. Kim, T. Jeong, et al., "Activating the Mn Single Atomic Center for an Efficient Actual Active Site of the Oxygen Reduction Reaction by Spin-State Regulation," *Journal of the American Chemical Society* 146, no. 49 (2024): 34033–34042, https://doi.org/10.1021/jacs.4c13137.

57. L. Hao, T. Yu, C. Liu, J. You, and R. Guo, "Modulation of Electron Transfer Behavior on Fe_2P-Co_2P/NPC Oxygen Electrocatalyst by Lattice Cation Substitution Engineering and Charge Transport Network Design for Rechargeable Zn-air Batteries," *Energy Storage Materials* 72 (2024): 103723, https://doi.org/10.1016/j.ensm.2024.103723.

58. M. Guo, L. Wang, Z. Huang, H. Li, T. T. Isimjan, and X. Yang, "Modulating the Energy Barrier via the Synergism of Cu_3P and CoP to Accelerate Kinetics for Bolstering Oxygen Electrocatalysis in Zn-Air Batteries," *ACS Nano* 18, no. 27 (2024): 17901–17912, https://doi.org/10.1021/acsnano.4c04479.

59. C.-Y. Wang, L. Zhang, J.-J. Feng, Y.-J. Gao, and A.-J. Wang, "Mo_2N Nanoclusters and FeMo Dual Atomic Active Sites Confined in N-doped Hollow Carbon Nanocages for Synergistic Improvement in Oxygen Reduction and Zn-air Battery," *Chemical Engineering Journal* 507 (2025): 160442, https://doi.org/10.1016/j.cej.2025.160442.

60. Q. Chang, F. He, Z. Zhang, et al., "Self-Organized Integrated Electrocatalyst on Oxygen Conversion for Highly Durable Zinc-Air Batteries," *Angewandte Chemie International Edition* 64, no. 4 (2025): e202416664, https://doi.org/10.1002/anie.202416664.

61. Y. Song, C. Han, W. Li, et al., "Engineering Bimetallic Cluster Architectures: Harnessing Unique 'Remote Synergy Effect' Between Mn and Y for Enhanced Electrocatalytic Oxygen Reduction Reaction," *eScience* 5, no. 3 (2024): 100332, https://doi.org/10.1016/j.esci.2024.100332.

62. M. Liu, J. Zhang, H. Su, et al., "In Situ Modulating Coordination Fields of Single-Atom Cobalt Catalyst for Enhanced Oxygen Reduction Reaction," *Nature Communications* 15, no. 1 (2024): 1675, https://doi.org/10.1038/s41467-024-45990-w.

63. M. Li, G. Han, F. Tian, et al., "Spin-Polarized PdCu–Fe_3O_4 In-Plane Heterostructures With Tandem Catalytic Mechanism for Oxygen Reduction Catalysis," *Advanced Materials* 36, no. 49 (2024): 2412004, https://doi.org/10.1002/adma.202412004.

64. Z. Zhang, Z. Zheng, N. Ma, et al., "Composition Tuning and Heterostructure Construction of Fe-Doped Co-Ni Hydroxide Nanosheets for Boosting Oxygen Electrocatalysis in Rechargeable Zn-air Batteries," *Chemical Engineering Journal* 509 (2025): 161248, https://doi.org/10.1016/j.cej.2025.161248.

65. L. Hao, T. Yu, X. Liu, et al., "Electronic Structure Modulation and Substance Transfer Acceleration Induced by Synchronous Construction of a Tri-Functional Electrocatalyst With Host–Guest Role Swapping in Zinc-Air Batteries," *Chemical Engineering Journal* 511 (2025): 161942, https://doi.org/10.1016/j.cej.2025.161942.

66. T. Chen, Y. Xu, D. Meng, et al., "Nest-Type NCM ⊂ Pt/C With Oxygen Capture Character as Advanced Electrocatalyst for Oxygen Reduction Reaction," *Journal of Energy Chemistry* 71 (2022): 304–312, https://doi.org/10.1016/j.jechem.2022.03.017.

67. Z. Luo, J. Gong, Q. Li, et al., "Geometric and Electronic Engineering in Co/VN Nanoparticles to Boost Bifunctional Oxygen Electrocatalysis for Aqueous/Flexible Zn-Air Batteries," *Chemistry - A European Journal* 30, no. 20 (2024): e202303943, https://doi.org/10.1002/chem.202303943.

Supporting Information

Additional supporting information can be found online in the Supporting Information section.
Supporting Information S1: rar270023-sup-0001-suppl-data.doc.